Journal of Materials Processing Tech. 304 (2022) 117533

Contents lists available at ScienceDirect

Journal of Materials Processing Tech.

journal homepage: www.elsevier.com/locate/jmatprotec

Effect of spattering on formation mechanisms of metal matrix composites in laser powder bed fusion

Li Shuai [a,b], Jiang Qinghong [b], Guo Sai [b], Zhang Bi [a,b,*], Zhou Cong [b]

[a] School of Mechatronics Engineering, Harbin Institute of Technology, Harbin 150001, China
[b] Department of Mechanical and Energy Engineering, Southern University of Science and Technology, Shenzhen 518055, China

ARTICLE INFO

Associate Editor: Erhan Budak

Keywords:
Metal matrix composite
Laser powder bed fusion
Grinding wheel
Diamond spattering
Balling phenomenon

ABSTRACT

Metal matrix composites (MMCs) with specially designed structures can be fabricated by laser powder bed fusion (LPBF) time-efficiently and cost-effectively, but reinforcements pose enormous challenges to the technique. In this work, the effect of reinforcement on the formation of MMCs in LPBF is studied by taking diamond grinding wheels (GWs) as an example. Based on the balling phenomenon observed in the LPBF process, the formation characteristics of GWs such as surface morphology, porosity, and flexural strength are investigated. The balling size is increased with an increase in the linear energy density of the laser beam due to more intense diamond spattering. The acting forces applied by the plume and ambient gas flow generated around the melt pool on a diamond grain are analyzed to investigate the generation of diamond spatter. For MMCs with coarse reinforcements, spattering is the dominant cause of the balling phenomenon due to the induced discontinuous melt tracks and uneven powder layers. Furthermore, the performance of a cup-type diamond GW fabricated by LPBF in the electrical discharge grinding (EDG) process of reaction-bond silicon carbide (RB-SiC) is evaluated by the surface and subsurface quality. The grinding process removes the resolidified layer of RB-SiC induced during the electrical discharging process and suppresses crack generation in the subsurface. The results presented in this study reveal the influence of diamond grains on the formation mechanism of GWs, which is also suitable for MMCs with coarse reinforcements.

1. Introduction

Laser powder bed fusion (LPBF) is one class of laser-based additive manufacturing (AM) technologies and is capable of producing complex products based on the layer-by-layer fusion strategy. Due to the higher flexibility compared with traditional manufacturing, LPBF has been applied to many industries including biomedical, aerospace, automotive, and so on (Hojjatzadeh et al., 2019). With the development of LPBF technology, research efforts are still being made to solve intractable industrial problems and expand its applications by structural optimization, material design, and process improvement (Khmyrov et al., 2016). The AM technologies have been explored to fabricate metal matrix composites (MMCs) with complex structures which are difficult to be produced by powder metallurgy or liquid state methods (Sharma et al., 2019). The AM technologies also offer manufacturers the ability to produce functionally graded and customized MMCs with shorter processing workflows and lower overall cost (Traxel and Bandyopadhyay, 2021; Kumar and Czekanski, 2017). Especially, LPBF has shown a great potential in the fabrication of MMCs with particular structures with higher geometric and dimensional accuracies as compared to directed-energy-deposition (DED) (Traxel and Bandyopadhyay, 2019).

A diamond grinding wheel (GW) is a typical example of an MMC, which is widely used as the last step of a manufacturing chain to control the dimensional accuracy and surface finish of an industrial part (Li et al., 2021). Bond materials work as the matrix, and abrasives such as SiC, cBN, and diamond grains are reinforcements used for removing materials from a workpiece. Pores play an important role in accommodating debris and grinding coolant, as well as suppressing temperature rise and workpiece burn in the grinding process (Tian et al., 2018). With the increasing demand on the grinding quality of industrial products, textured GWs with complex structures or profiles have been proposed to improve the grinding performance(Li and Axinte, 2016). Considering the capability of producing complex structures layer by layer, LPBF provides an efficient and cost-effective solution to fabricating textured GWs (Spierings et al., 2015).

Previous studies have proved the feasibility of GWs fabricated in

* Corresponding author at: Department of Mechanical and Energy Engineering, Southern University of Science and Technology, Shenzhen 518055, PR China.
E-mail address: zhangb@sustech.edu.cn (Z. Bi).

https://doi.org/10.1016/j.jmatprotec.2022.117533
Received 11 December 2021; Received in revised form 10 February 2022; Accepted 13 February 2022
Available online 17 February 2022
0924-0136/© 2022 Elsevier B.V. All rights reserved.

LPBF with different bond materials. Tian et al. applied the selective laser melting (SLM) technique to fabricating porous aluminum-bond GWs with various cellular structures (Tian et al., 2019). The porosity ratio ranging from 30% to 70% could be controlled by the strut diameters (Tian et al., 2020). Due to the high porosity ratio, slighter work hardening was induced by the fabricated GWs compared with the electroplated GWs. Du et al. (2019) introduced internal cooling holes in a resin-bond diamond GW by selective laser sintering (SLS) which is similar to LPBF. The grinding forces were reduced in grinding of glass and cemented carbide with the printed GW. Wu et al. (2019) built a CoCrMo bond diamond-impregnated bit with a grid-shaped matrix in LPBF to improve the efficiency of drilling hard rocks. During the laser scanning process, the bond materials containing Ti or Cr could react with diamond grains and generate carbide at the interface, thus increasing the bonding strength. Gan et al. (2020) found that TiC was formed around the diamond grains in the fabrication of CuSnTi bonded diamond abrasive composites in SLM, resulting in the enhanced wear-resistant property as compared with the hot-pressed sintered counterpart. Similarly, Denkena et al. (2020) also found the existence of TiC in the interface of nickel-titanium bond and diamond grains in the grinding layer fabricated by LPBF. Due to the formation of TiC, the grain retention forces were high enough to produce continuous scratch paths with no abrasive breakage in the scratching test on the cemented carbide. Besides the porosity ratio and morphology, LPBF possesses the capability of controlling abrasive arrangement. Yang et al. (2016) controlled the diamond grains distribution in the powder layer and fabricated GW with the regularly distributed grains in three dimensions.

Similar to other MMCs, the fabrication of diamond GWs in LPBF encounters great difficulties, including the incurrence of pores, interface cracks between reinforced particles and metal matrix (Li et al., 2021), and thermal residual stress (Constantin et al., 2021). The reinforcements have a negative effect on the densification behavior in LPBF. Balling phenomenon is considered as one of the causes of pores in the LPBF of MMCs due to the increased viscosity by the reinforcements (Ma et al., 2019). For MMCs with a higher volume fraction of the reinforcements, the balling phenomenon would be more prominent. In the fabrication of GWs with 25 vol% diamond grains, severe balling materials were observed on the top surface, resulting in many large pores (Denkena et al., 2020). Even though pore is an essential element in GWs, large pores are undesirable because of the reduced mechanical strength of fabricated material. It was reported that an increased laser energy density allows fabricating denser parts (Mao et al., 2018). Nevertheless, an excessive laser energy input would cause higher thermal residual stress and cracks between the reinforced particles and the metal matrix due to the distinct thermal expansion coefficients (Constantin et al., 2021). The balling phenomenon caused by the reinforcements may also be associated with particle spattering. In the fabrication of MMCs, the reinforcements may turn into spatters under the impact of high-speed metal vapor in LPBF, especially for the infusible reinforcements. Li et al. (2022) observed the diamond spattering in the fabrication of GWs in LPBF and revealed the detrimental effect on the formation quality. Coarser reinforcements may induce more prominent spattering phenomenon. Due to the larger diamond grains and higher volume percentage, spattering plays a critical role in the balling phenomenon in the LPBF of GWs. However, there are few studies on the spattering behavior of reinforcements and its effect on the formation mechanisms of MMCs in LPBF.

To investigate the effect of spattering on the formation mechanisms of MMCs in LPBF, the formation characteristics of bronze-bond GWs with 10 vol% diamond grains are studied with a consideration of diamond spattering. The surface morphology, porosity ratio, pore morphology, and flexural strength of diamond GWs with different processing parameters (laser power and scanning velocity) are studied in terms of the balling phenomenon. The study then theoretically analyzes the generation mechanism of diamond spatters by considering the interactions between the laser plume, melt pool, and diamond grains. It estimates the forces acting on the diamond grains by the plume and dynamic flow field around the melt pool. The effect of diamond spattering on the formation mechanism of GWs is also studied through analysis on the surface morphology evolution. The study further performs electrical discharge grinding (EDG) of reaction bonded silicon carbide workpiece (RB-SiC) with a cup-type diamond GW fabricated by LPBF. The grinding performance of the cup-type diamond GW is studied in comparison to a bronze alloy grinding tool in terms of surface roughness and morphology of the workpiece. Conclusions are drawn for the study.

2. Materials and methods

2.1. Materials and LPBF processes

Globular CuSn10 alloy powders with particle sizes from 5 μm to 53 μm were used as the bond material. The particle size distribution of the CuSn10 alloy powders is shown in Fig. 1(a). Diamond abrasive were with irregularly truncated octahedron grains ranging from 38 μm to 45 μm which were consistent with that of the CuSn10 alloy powders to avoid unevenness of the mixed powder layer. The diamond abrasive grains at a volume percentage of 10% were mixed thoroughly with the CuSn10 alloy powders in a 3D mixer. The mixed powders are shown in Fig. 1(b).

Diamond GWs were fabricated with the mixed powders in an LPBF equipment (Dimetal-100, Guangzhou Laseradd Technology Co., Ltd., China) with a maximum laser power of 500 W. The formation schematic diagram is depicted in Fig. 1(c). An orthogonal scanning strategy was employed in the LPBF process to build the diamond GWs. The Gaussian laser beam diameter was around 120 μm and all the experiments were conducted in a printing chamber filled with Argon (oxygen content $<$ 0.1%). Cubic abrasive segments with an edge length of 8 mm were first built at three different laser power levels ($P = 100$, 140, 180 W) and three scanning speeds ($V = 1000$, 1500, 2000 mm/s). The hatch space and layer thickness were kept constant at 60 μm and 30 μm, as listed in Table 1. For comparison with abrasive segments, three cubic CuSn10 alloy specimens were built by LPBF at $P = 180$ W and $V = 1000$, 1500, 2000 mm/s.

2.2. Characterization of the diamond abrasive segments

The top-surface morphology and roughness of the as-built abrasive segments were measured by the confocal laser scanning microscopy (Keyence, VK-X1000). In this study, only open pores were concerned and the Archimedes method was used to measure the porosity ratio of the abrasive segments. The morphology and distribution of the pores inside the as-built abrasive segments were investigated through a cross-sectional analysis by the ultra-depth 3D optical microscope (Keyence, VHX-7000).

To measure the flexural strength of the abrasive segments, a three-point bending test was performed to characterize the mechanical strength of GWs (Tian et al., 2019). The bending specimens were fabricated in a chessboard strategy first and were then ground to remove the rough layer of all the external surfaces. The length, width, and thickness of the bending specimens were machined to 36 mm, 4 mm, and 3 mm, respectively, and chamfer with a size of 0.12 ± 0.05 mm was machined on each edge, as shown in Fig. 2(a). The specific fixture for the three-point bending test is shown in Fig. 2(b), consisting of a ruler, supporting rods, and load rod. The span of supporting rods was adjusted to 30 mm through the ruler. The bending specimens were placed on the supporting rods symmetrically and the load rod interacted with the middle of specimens and moved down at the speed of 0.5 mm/min. The force-displacement curve was obtained and the critical load for fracture was determined. The macro and micro fracture surfaces were characterized by a field emission scanning electron microscope (SEM, Zeiss Merlin).

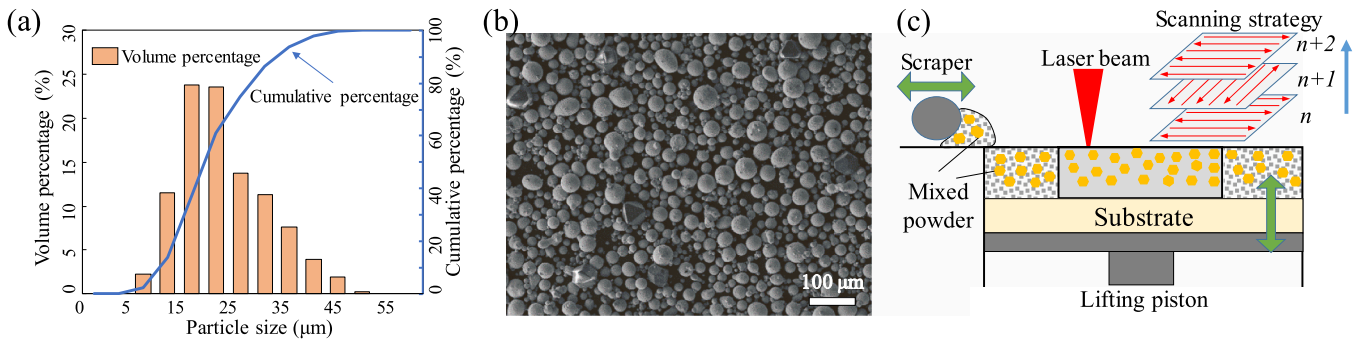

Fig. 1. (a) Particle size distribution of the CuSn10 alloy powders, (b) SEM image of the mixed powders, and (c) schematic diagram for the LPBF process.

Table 1
LPBF processing parameters for abrasive segments.

Processing parameters	CuSn10/Diamond	CuSn10
Laser spot size, σ (μm)	120	120
Powder layer thickness, h (μm)	30	30
Hatch spave, w (μm)	60	60
Laser power, P (W)	100, 140, 180	180
Scanning velocity, V (mm/s)	1000, 1500, 2000	1000, 1500, 2000

3. Formation characteristics of the as-built GWs

3.1. Morphological properties

The 3D surface morphology of the as-built abrasive segments is presented in Fig. 3(a). In the macroscopic view, long bulges were formed in the initial region along the moving direction of the scraper under the process conditions of $P = 100$ W, $V = 1500$, 2000 mm/s and $P = 140$ W, $V = 2000$ mm/s. Linear Energy Density (LED), which is defined as the ratio of the laser power and scanning velocity, exerted considerable influence on the surface morphology of the abrasive segments. The height of the long bulges reached the maximum around 0.21 mm with the lowest LED value, i.e., 0.05 J/mm at $P = 100$ W, $V = 2000$ mm/s. With the increase of LED value, the bulges vanished and the top surfaces became flat. At a low LED value, the partially melted CuSn10 alloy powders generated a large number of pores inside the as-built layers. Due to the pores, the as-built layers were slightly thicker than the set value of layer thickness, which was observed to block the scraper in the powder spreading process. The right abrasive segment edge caused elastic deformation and spring-back of the rubber scraper, resulting in few powders spread over the initial region. After the formation of several layers, remelting occurred in the initial region, the as-built layers became denser but detached from the previously deposited materials due to the excessive thermal residual stress. With the deposition of materials, the detached layers evolved into bulges.

Balling materials were observed on the top surface of all the abrasive segments, shown in Fig. 3(a) and result in a rough surface. Adjacent balling materials interconnected with each other and caused bridging materials, which induced many pits on the surface, as exhibited in the magnified optical graphs in Fig. 3(b). Overall, an increase in laser power or a decrease in scanning velocity could contribute to a rougher surface with larger balling materials. As shown in the three-dimensional topography, the sizes of the balling materials and pits were increased with the LED value in general. In particular, the maximum diameter of the balling materials at $P = 180$ W, $V = 1000$ mm/s was around 500 μm, which is significantly larger than those at $P = 100$ W, $V = 2000$ mm/s; and $P = 140$ W, $V = 1500$ mm/s. As for the as-built CuSn10 alloy, balling materials were also observed at the top surface, with a much smaller height and dimension as compared to the abrasive segments, as shown in Fig. 3(c).

The surface roughnesses Sa and Sz of the as-built abrasive segments, representing the arithmetic mean and maximum height of the surface profile, were measured and are shown in Fig. 4(a). As LED was less than 0.1 J/mm, Sa and Sz fluctuated at around 40 μm and 430 μm, respectively. When LED was larger than 0.1 J/mm, an increasing trend of both Sa and Sz with LED value was obtained. The maximum Sa and Sz were around 84.56 μm and 910.43 μm at the maximum LED of 0.18 J/mm. The increase of surface roughness was attributed to the increased balling

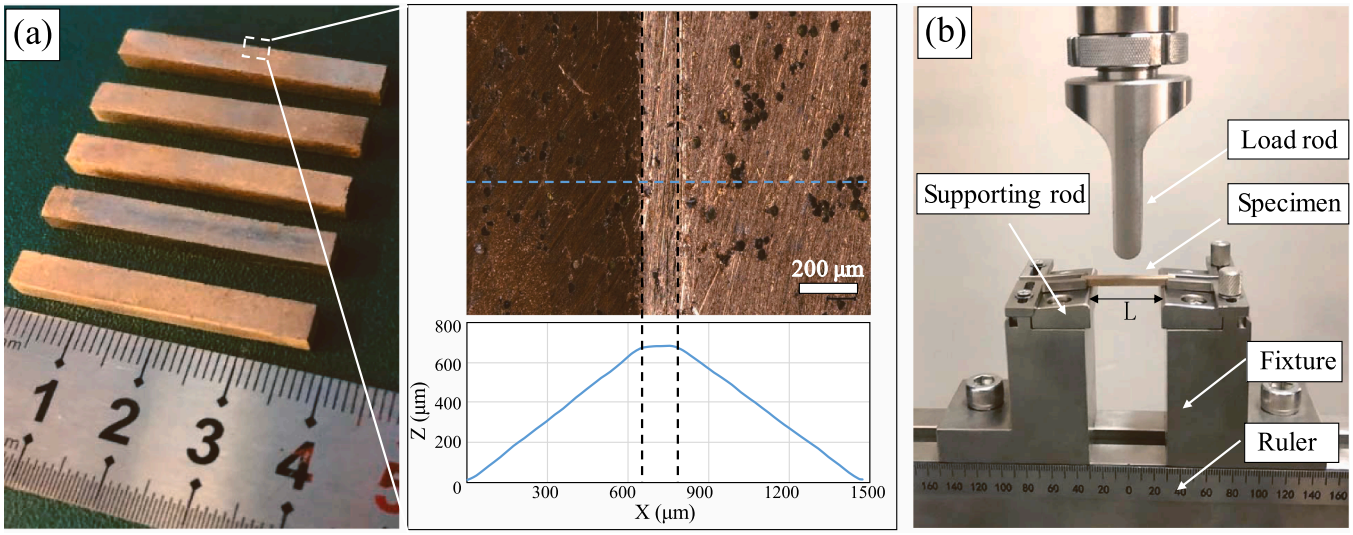

Fig. 2. Three-point bending test: (a) as-built diamond abrasive bending specimens; and (b) bending equipment.

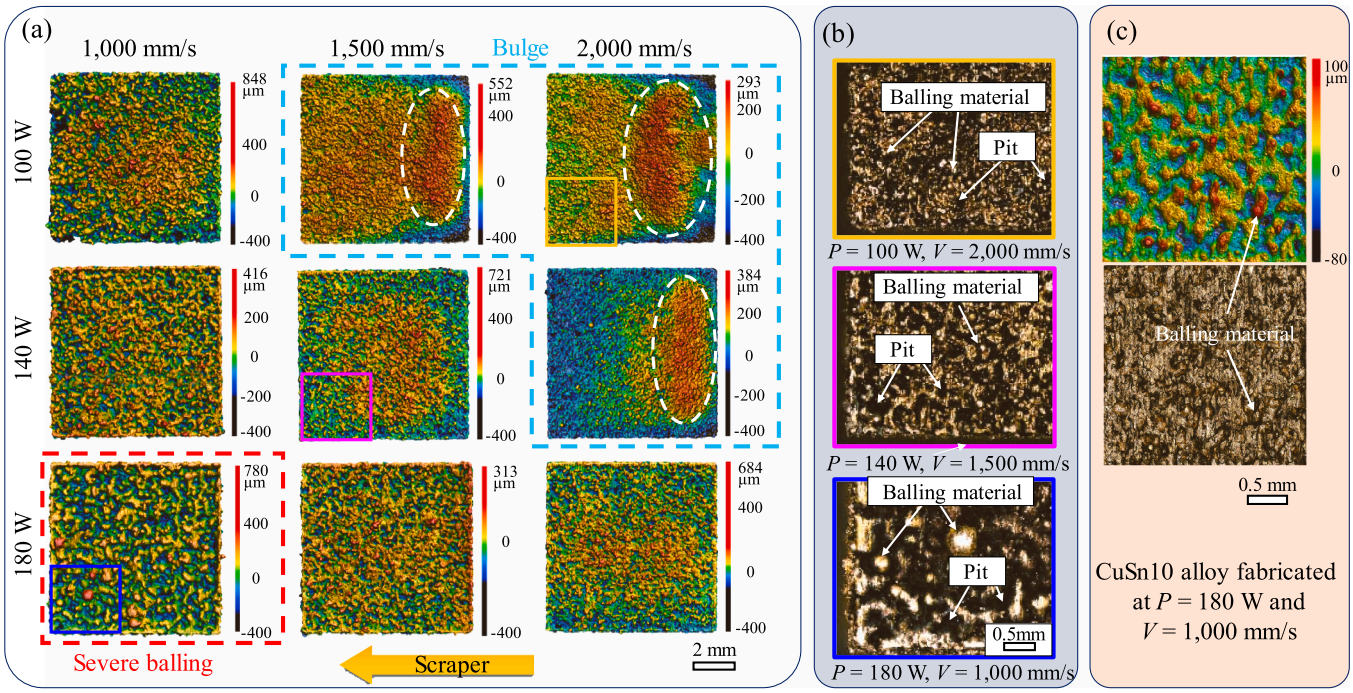

Fig. 3. (a) Macro three-dimensional topography of the as-built abrasive segments, (b) corresponding magnified optical graphs in the left corner of the as-built abrasive segments; (c) topography of CuSn10 alloy fabricated at $P = 180$ W, $V = 1000$ mm/s for comparison.

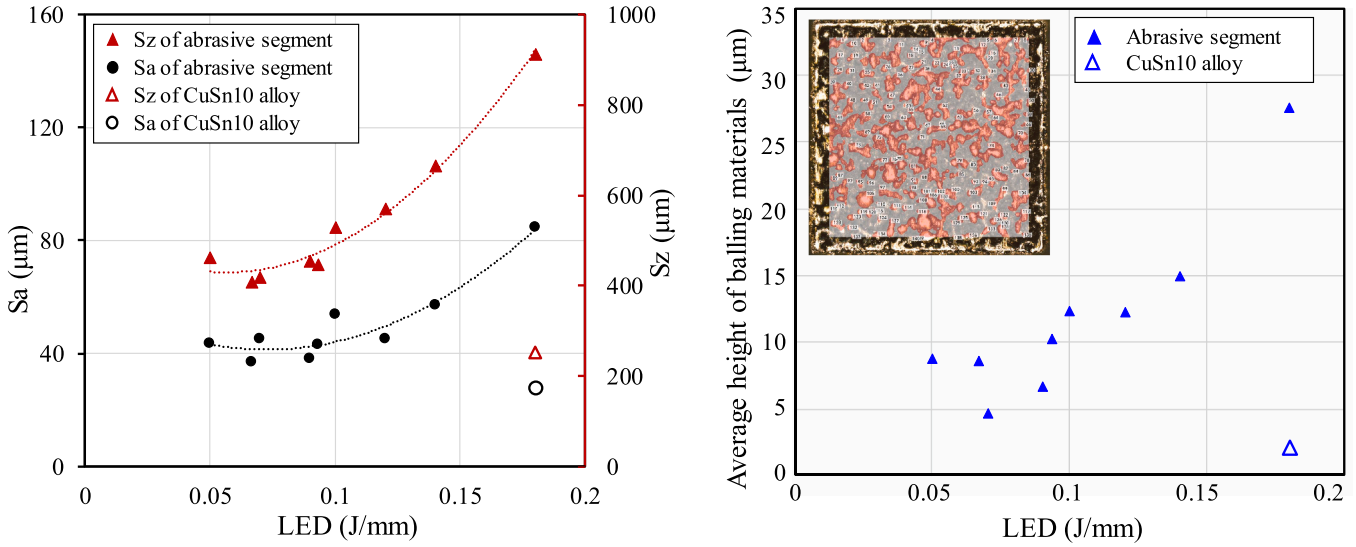

Fig. 4. Variations in surface roughness Sa and Sz (a) and the average height of the balling materials (b) with LED.

size, as observed in Fig. 3. To evaluate the balling level of the as-built abrasive segments, the average height h_{av} of the balling materials which is defined as the ratio of the total volume of material higher than 30 μm above the horizontal plane (total volume of the red island area in Fig. 4(b)) to the measured area is proposed in this study. As shown in Fig. 4(b), the changes of h_{av} with LED resembled the variations of surface roughness with LED, indicating that the balling materials had a direct influence on the surface quality. Surface roughness was increased with the balling level because higher peaks and deeper cavities were formed with larger balling materials.

3.2. Porosity ratio

Due to the balling phenomenon in the fabrication process, many pores were formed inside the abrasive segments, which are essential and preferred in a GW. The porosity of each as-built abrasive and CuSn10 alloy segment was measured three times, and the average results are shown in Fig. 5(a). Abrasive segments with a porosity ratio larger than 20% were fabricated in this study. With the increase of LED, the porosity ratio was first decreased from 30.43% at LED = 0.05 J/mm to 21.15% at LED = 0.09 J/mm. As further increasing LED, the porosity ratio was increased slightly to 25.35% at LED = 0.18 J/mm. However, an opposite trend of the porosity ratio of the as-built CuSn10 alloy segments was observed. The porosity ratio decreased almost linearly from 17.52% to 4.33% as LED increased from 0.09 J/mm to 0.18 J/mm. As the absorptivity of the CuSn10 alloy to the laser beam with a wavelength of 1064 nm was relative low, the powders were melted more thoroughly at an increased laser energy density, thus the density of the CuSn10 alloy

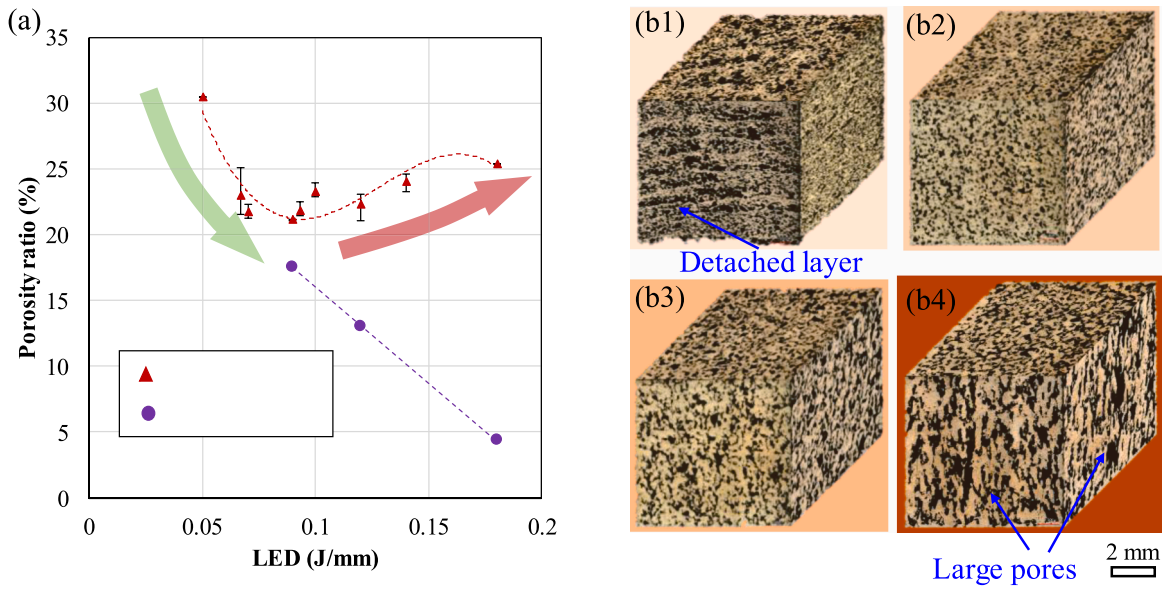

Fig. 5. Effect of LED on (a) porosity ratio and (b) pore morphology inside the as-build abrasive segment: (b1) $P = 100$ W, $V = 2000$ mm/s (LED = 0.05 J/mm); (b2) $P = 180$ W, $V = 2000$ mm/s (LED = 0.09 J/mm); (b3) $P = 140$ W, $V = 1000$ mm/s (LED = 0.14 J/mm); (b4) $P = 180$ W, $V = 1000$ mm/s (LED = 0.18 J/mm).

was enhanced (Mao et al., 2018). However, in the LPBF process of the diamond abrasive segments, diamond grains caused more pore formation. Upon the laser beam passing by a diamond grain, the diamond grain was ejected by the metal vapor induced by the evaporation of the CuSn10 alloy, leading to the diamond spattering phenomenon with a crackling sound. Diamond spattering helped create porosities within the abrasive segments. The quantity of the diamond spatters was increased with an increased LED value, and thus a slight increase in the porosity ratio of the as-built abrasive segments is observed in Fig. 5(a).

The pore morphology was found to vary at different laser energy densities. To reveal the pore morphology inside the as-built abrasive segments, cross-sections parallel and perpendicular to the building direction were mechanically ground by the SiC grinding papers of 600, 1000, 2000 grits, sequentially, and finally polished by a SiO_2 slurry. As shown in Fig. 5(b), the shape and size of the pores differed at different LED values. With an insufficient input of laser energy, such as LED = 0.05 J/mm, both the insufficiently melted CuSn10 powders and the diamond spatters determined the pore morphology. The insufficiently melted powders introduced a large number of small pores inside the as-built abrasive segment. Due to the diamond spattering, several large pores were also generated randomly. Besides pores, detachment of the as-deposited layers was induced due to a weak interlayer bond strength at LED = 0.05 J/mm, as shown in Fig. 5(b1). The detached layers bulged under the cycling thermal stresses and evolved into long bulges on the top surface which is observed in Fig. 3(a). Both the induced pores and the detachment led to the largest porosity ratio of 30.43%. As LED was increased to 0.09 J/mm (Fig. 5(b2)), the bond materials could be melted thoroughly and the detached layers disappeared. The pores were more evenly distributed inside the as-built abrasive segment as compared to the other segments. At LED = 0.09 J/mm, a relative balance was achieved between melting of the bond materials and spattering of the diamond grains. Thus, the porosity ratio decreased to the lowest value. With a further increase in LED, severer diamond spattering was triggered and formed larger balling materials, as presented in Fig. 3(a). Some large pores with a feature size around hundreds of microns were induced and the porosity ratio was increased slightly (Fig. 5(b3)). As LED was increased to 0.18 J/mm, pores became even larger (on the order of millimeters) and extended along the building direction on the order of millimeters, as shown in Fig. 5(b4). Pores were significantly longer in the cross-section parallel to the building direction than those perpendicular to the building direction. In the cross-section perpendicular to the building direction, the bond materials were with an island-like distribution surrounded by the interconnected pores due to the balling phenomenon.

3.3. Flexural properties and fracture analysis

The flexural properties of all the abrasive specimens were measured in the three-point bending test (Tian et al., 2020; Ding et al., 2013). The force-displacement curves of four abrasive specimens with different processing parameters are shown in Fig. 6(a). The forces increased with the displacement to the peak value at the elastic deformation stage, then rapidly dropped as cracks were generated. As depicted in Fig. 6(b), the cracks of all the specimens were observed in the middle of the bottom surface as the displacement reached around 0.5 mm. Due to the ductility of the CuSn10 alloy, cracks propagated slowly to the top surface and the forces declined gradually with the bending displacement until the specimens were fractured. The abrasive specimens with different processing parameters showed the distinct flexural properties. The gradient of the force-displacement curve, which is defined as flexural modulus, and the flexural force of the specimens fabricated at LED = 0.09 J/mm were larger than the counterparts of the other specimens. The specimens fabricated at LED = 0.14 J/mm showed the lowest strength.

The flexural strength can be calculated by the peak force with the following equation (Tian et al., 2020):

$$\sigma_f = \frac{3PL}{2bh^2} \tag{1}$$

where σ_f is flexural strength; P is the peak force for fracture; L is the span of the two supporting rods; b and h are specimen width and thickness, respectively. Width b and thickness h near the fracture point were measured with a Vernier caliper.

Three specimens were tested for each set of the fabrication parameters, and the average values are displayed in Fig. 7. The flexural strength of the as-built abrasive specimens first increased with LED and then decreased rapidly as LED was higher than 0.10 J/mm. The flexural strength reached the highest value of 213.37 MPa at LED = 0.09 J/mm with the lowest porosity ratio. As LED was increased to 0.1 J/mm, the flexural strength dropped to only 92.29 MPa. An increased LED further reduced the flexural strength of the specimens significantly. Based on the previous studies, the flexural strength was closely related to the pores inside a GW. As depicted in Fig. 7(b), the flexural strength was

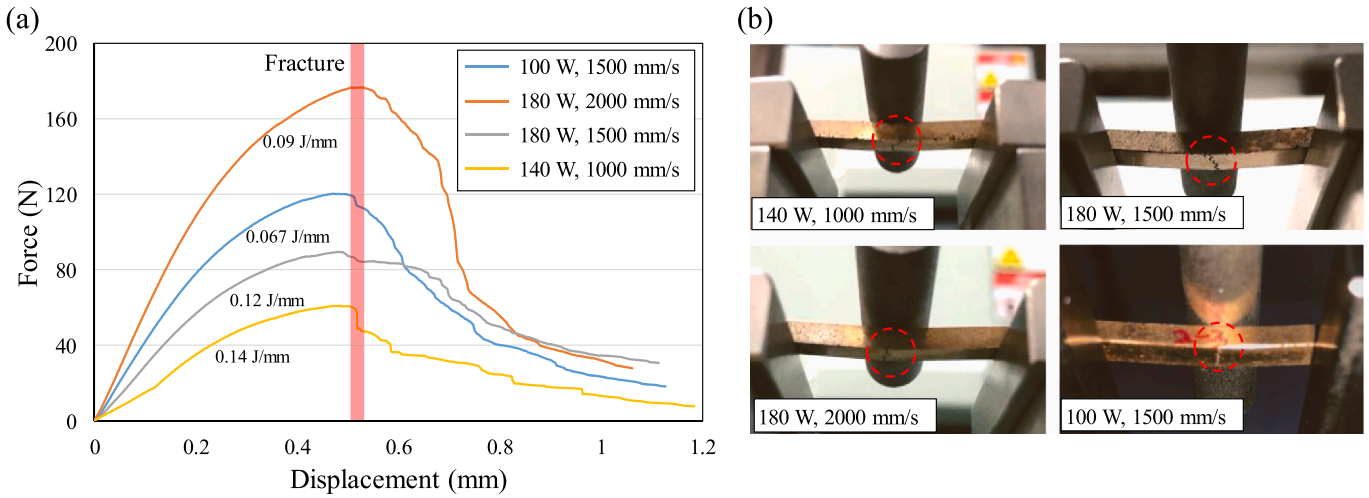

Fig. 6. (a) Flexural force-displacement curves and (b) crack location of the as-built abrasive specimens.

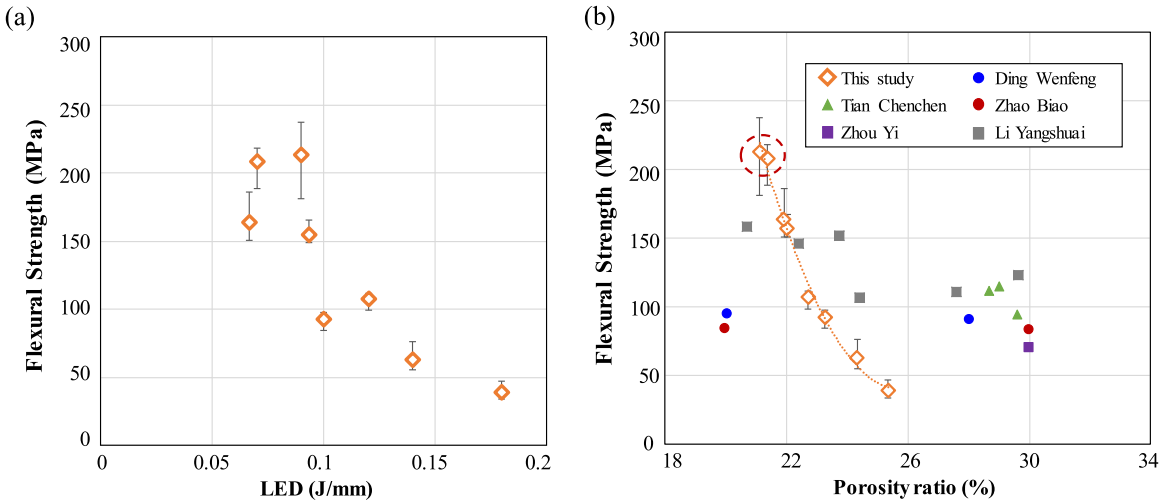

Fig. 7. Variations of flexural strengths with LED (a) and porosity ratio (b). The flexural strength decreases with porosity. The maximum flexural strength is higher than that of the other porous GWs in the previous studies (Tian et al., 2018; Ding et al., 2013; Zhou et al., 2020; Zhao et al., 2019; Li et al., 2011).

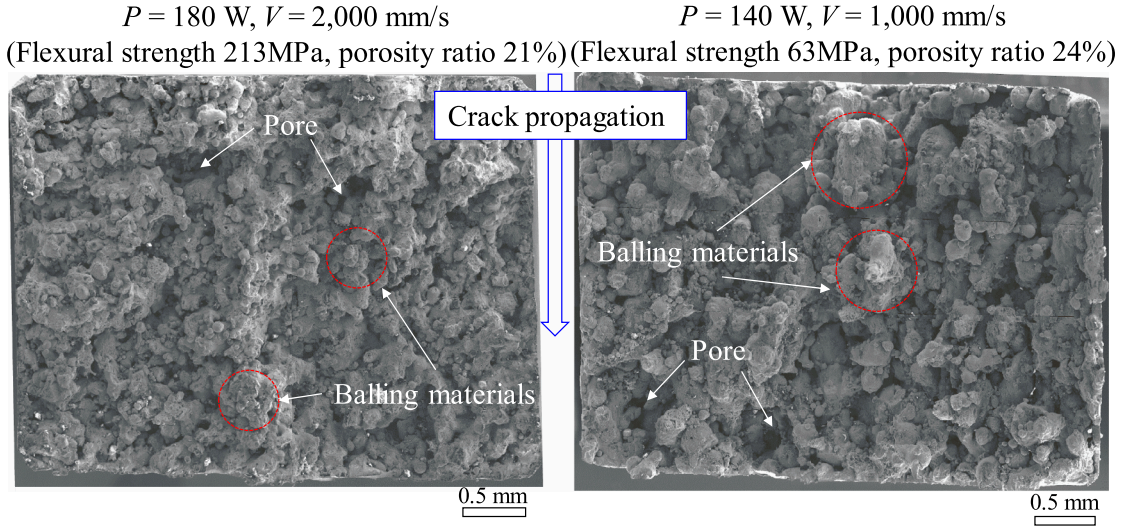

Fig. 8. Macroscopic fracture morphologies of the abrasive specimen fabricated at (a) $P = 180$ W, $V = 2000$ mm/s with flexural strength of 213 MPa, porosity ratio of 21%, (b) $P = 140$ W, $V = 1000$ mm/s with flexural strength of 63 MPa, porosity ratio of 24%.

decreased almost linearly with the porosity ratio. The maximum flexural strength in present study was higher than that of the other porous GWs in the previous studies (Tian et al., 2018; Ding et al., 2013; Zhou et al., 2020; Zhao et al., 2019; Li et al., 2011), which indicates that the as-built GW can meet the requirement in strength.

The pore morphology exerted a great influence on the flexural strength. When the LED value was high enough to melt the CuSn10 alloy powders thoroughly, dense and evenly distributed pores were formed within an abrasive specimen. However, large pores induced by severe diamond spattering with an excessive LED seriously reduce the flexural strength. This can be confirmed by the fracture analysis on the abrasive specimens, as shown in Fig. 8. In the macroscopic images of the two specimens fabricated at LED = 0.09 J/mm and 0.14 J/mm, rough and uneven fracture morphologies with a large number of balling materials and pores were observed, showing a porous structure of the as-built abrasive specimens. On the whole, the balling size of the specimen at LED = 0.14 J/mm was larger than that of the specimen at LED = 0.09 J/mm, resulting in a higher porosity ratio. Some large pores were observed in the fracture of the specimens at LED = 0.14 J/mm. The balling materials connected with the adjacent materials and resulted in the bridging phenomenon. The flexural strength of the porous abrasive specimens was determined by the bridging bond materials. Smaller balling materials helped increase the number of bridging materials, leading to a higher flexural strength. Larger balling materials induce large pores which significantly deteriorate the strength of the abrasive specimen.

Fig. 9 shows the microscopic fracture morphology of the bridging bond materials. The fractured region shows a dimple feature with many small spherical pores, indicating that the fracture mechanism was a ductile fracture (Wang et al., 2020). The size of the spherical pores approximately ranged from 2 μm to 8 μm. According to the previous studies, the spherical pores were mainly ascribed to the evaporated alloy gas or the original ambient gas trapped inside the melted alloys (Khairallah et al., 2016). As illustrated in Fig. 9(c), the surfaces of the spherical pores were quite smooth with a number of the closely arrayed cellular grains smaller than 1 μm due to the surface tension during the solidification process. Meanwhile, the dimple size was in a range of 0.3–1 μm, similar to the cellular grain size shown in Fig. 9(b), indicating an intergranular fracture mode. The fractured cellular grains with different orientations were revealed in some areas. In Fig. 9(d), cellular grains perpendicular and parallel to the fracture surface are observed. The grain orientations were mainly affected by the heat flux and the melt flow driven by the Marangoni force. Through the fractured cellular grain morphology, the cellular grain size is measured as 0.3–0.6 μm, further verifying the intergranular fracture mode of the as-built abrasive specimens.

3.4. Bonding morphology of diamond grains

The bonding morphology of diamond grains was investigated through the analysis of fracture surface. As shown in Fig. 10, the diamond grains were mainly distributed in the pores of the abrasive specimens and surrounded by the balling bond materials. Due to the high surface energy of diamond to copper, bonding of the CuSn10 alloy to the diamond grains was weak (Wang et al., 2018). Diamond grains were physically held by the CuSn10 alloy. In some cases, a gap was formed between a diamond grain and the CuSn10 alloy, as depicted in Fig. 10 (b), which had a negative effect on the bonding strength of the GW. Compared with a dense GW, the bonding strength was inferior due to the incomplete wrapping of the diamond grains. Further studies should be conducted to explore the problem. With a proper LED value, the diamond grains could keep intact after being irradiated by the laser beam. Only a few melted CuSn10 alloy spots adhered to the surface of the diamond grains. However, with a high LED value, the diamond grains were more easily graphitized as the temperature reached the graphitization temperature (approximately 1500 °C in the vacuum or an inert gas environment (Gan et al., 2020)). Graphitization can greatly reduce the strength of the diamond and should be avoided in the LPBF process.

4. EDG with the as-built GWs

4.1. EDG experimental procedures

To evaluate the performance of the as-built diamond GW, EDG

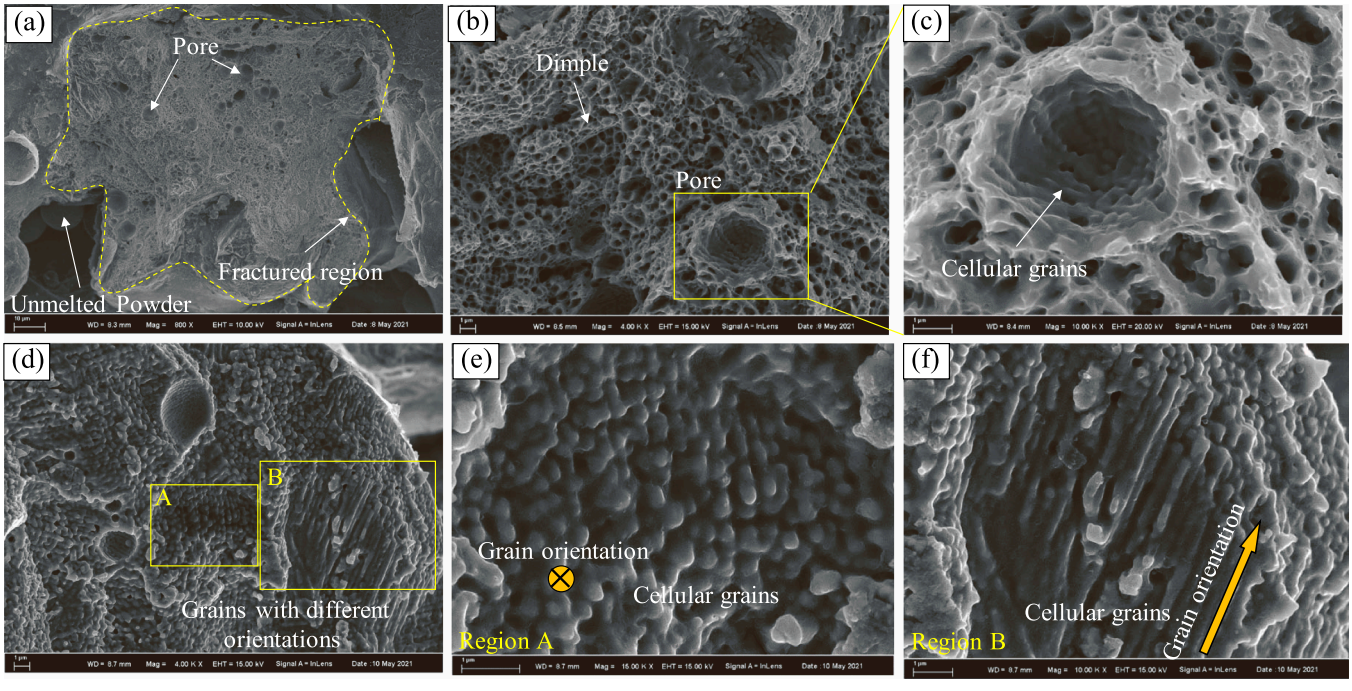

Fig. 9. Microscopic fracture morphology of the bridging bond materials, (a-c) morphology of the dimples and spherical pores; (d-f) morphology of the fractured cellular grains with different orientations.

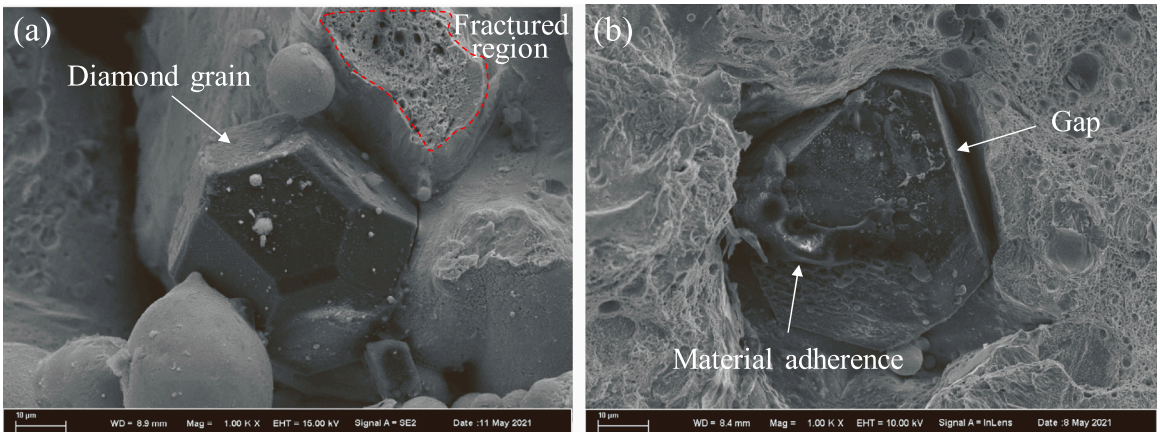

Fig. 10. Bonding morphology of the diamond grains in the abrasive specimens fabricated at $P = 180$ W, $V = 2000$ mm/s.

experiments were performed on an electrical discharge machine (Sodick, AL40G), as shown in Fig. 11(a). In the EDG experiments, a segmental cup-type GW was fabricated at $P = 180$ W and $V = 2000$ mm/s according to the comprehensive analysis on the formation of a diamond GW. As shown in Fig. 11(b), the substrate was machined and finally assembled into a segmental cup-type GW. The volume fraction of the diamond grains was 10 vol%. The dimensions of the segmental cup-type GW are listed in Table 2. For comparison, a similar CuSn10 alloy GW was also fabricated in LPBF with $P = 220$ W and $V = 1000$ mm/s. Before the EDG experiments, the end surfaces of the as-built GWs were dressed using a silicon carbide wheel.

The commercial RB-SiC provided by Goodfellow Cambridge Ltd. (UK) was used as workpiece material. The RB-SiC was fixed onto a steel plate, which was mounted on the electromagnetic worktable. The RB-SiC was connected to the positive pole while the grinding tool was connected to the negative pole of the power supply. The open-circuit voltages of 120 V and 200 V were employed to maintain the discharge process in EDG. The EDG processing parameters are shown in Table 2 in detail. All the experiments were conducted in a tank filled with the dielectric fluid.

Surface topography of the ground RB-SiC was observed via SEM and the confocal laser scanning microscopy. Surface roughness was measured by a probe profilometer (SURFCOM NEX 031 DX-12, SEIMITSU). For the subsurface characterization, a cross-section of the ground RB-SiC with a width of 30 μm was machined via a focused ion beam (FIB, FEI Helios 600i).

4.2. Surface topography of RB-SiC

Fig. 12 shows the surface topography of RB-SiC ground by the as-built diamond GW and CuSn10 alloy GW. The surface ground by the CuSn10 alloy GW was flat, but a uniform layer of resolidified materials

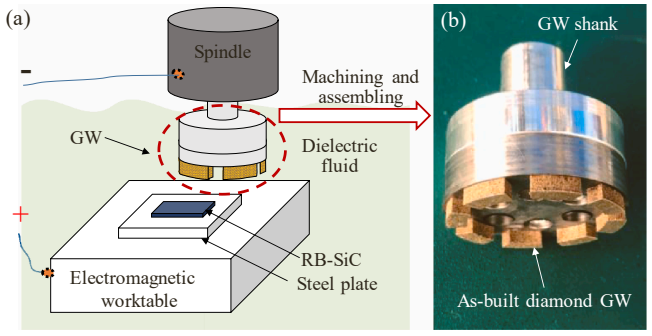

Fig. 11. (a) Schematic EDG experimental setup and (b) the as-built segmental cup-type GW.

Table 2
EDG conditions.

Parameter	Value
Grinding tool dimensions	diameter of D = 38 mm, width of B = 4 mm, 8 segments with 15° intervals
Grinding tool material	as-built diamond GW, CuSn10 alloy
Spindle speed (r/min)	300
Grinding depth (mm)	0.1
Polarity	Grinding wheel (-), RB-SiC (+)
Discharge voltage (V)	120, 200

with numerous craters was formed during the electrical discharge process, as illustrated in Fig. 12 (a) and (d). Under the thermal effect of discharge sparks, the local temperature could easily reach the melting point of RB-SiC (Rao et al., 2018). The melted RB-SiC was rapidly cooled in the dielectric fluid, resulting in a layer of the resolidified material with discharge craters on the surface (Rao et al., 2020). Unlike Fig. 12 (a), grinding tracks were induced in the surface ground by the as-built diamond GW, as shown in the macroscopic images of Fig. 12 (b) and (c). Under the combined effect of the electrical discharging and grinding, RB-SiC was melted first and removed by the subsequent diamond grains. Since only feed in the Z direction was applied in the EDG experiments, resolidified materials still existed in the zones with no grinding actions of the diamond grains, leading to the ridges on the ground surface. Discharge craters were also observed on both the ground surfaces. Compared with the surface topography of the RB-SiC ground at 120 V, the grinding tracks seemed to be flatter under the discharge voltage of 200 V.

The surface damages caused by the as-built diamond GW at 120 V and 200 V are shown in Fig. 12 (e) and (f). Due to the thermal softening effect by the discharge sparks, plastic deformation of RB-SiC occurred on the surface with some microgrooves. Brittle fracture was still the dominant type of surface damage at 120 V, because a large amount of material chipping was observed in the grinding zones in Fig. 12 (e). At 200 V, the grinding tracks became flatter and few brittle fracture was observed. A higher electrical discharge voltage could enhance the ductile grinding performance and reduce the fracture damage. However, the electrical discharge process was accompanied by the whole grinding process, EDM zones were also generated in the surface and interrupted the grinding tracks, as indicated by the yellow dashed frame shown in Fig. 12 (d) and (e).

Surface roughness was measured four times and the results are shown in Fig. 13 (a). Surface roughness Ra of RB-SiC ground by the diamond GW at 120 V and 200 V were 4.12 μm and 2.40 μm, respectively. Nevertheless, smaller Ra values, 1.21 μm at 120 V and 1.45 μm at 200 V, were obtained by the CuSn10 alloy GW. As the discharge voltage was increased from 120 V to 200 V, the surface roughness was decreased

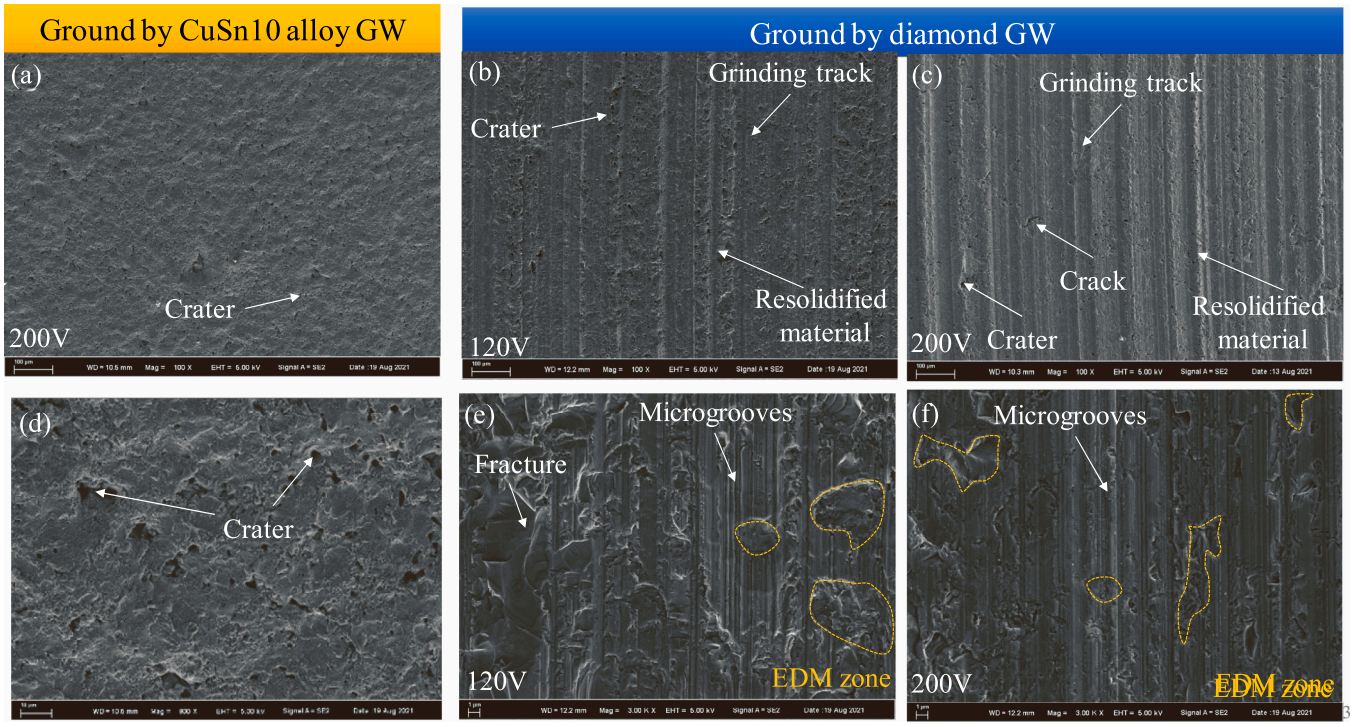

Fig. 12. Surface topography of RB-SiC ground by the CuSn10 alloy GW (a, d) and by the diamond GW (b, c, e, f). The voltages applied were 120 V (b, e) and 200 V (a, c, d, f).

when using the diamond GW but increased slightly when using the CuSn10 alloy GW. As shown in Fig. 13 (b-e), due to the diamond grinding action, grinding tracks were formed in the surface of RB-SiC, resulting in a higher Ra value. In the EDG process with the CuSn10 alloy GW, RB-SiC was removed only by melting and evaporation. The enhanced discharge voltage increased the amount of discharge craters, increasing the surface roughness slightly. However, in the EDG process with the diamond GW, the enhanced discharge voltage led to a larger discharge gap, thus the grinding depth of the diamond grains was decreased, resulting in shallower and flatter grooves. As illustrated in Fig. 13 (c) and (d), the largest height difference between the peaks and valleys was decreased from 23.48 μm at 120 V to 16.31 μm at 200 V. Furthermore, a higher discharge voltage could reduce fracture damage, as shown in Fig. 12.

4.3. Subsurface quality of RB-SiC

The cross-sections of the ground RB-SiC are shown in Fig. 14. A Pt layer was deposited on the ground surface to protect the ground workpiece. In Fig. 14 (a) and (b), a layer of the resolidified material was formed on the top surface with a thickness ranging from 0.31 μm to 1.04 μm, which is consistent with the surface observations in Fig. 12 (d). Remarkable voids were found in the resolidified material layer. In subsurface of RB-SiC ground by the CuSn10 alloy GW, two macro cracks were observed extending downward several microns. A zigzag crack with a depth of 3.97 μm was clearly presented in Fig. 14 (b). The resolidified material and cracks were caused by the thermal effect of discharge sparks and the induced high-level thermal stress. However, there were no resolidified material and cracks in the subsurface of RB-SiC ground by the diamond GW. On one hand, diamond grinding could remove the resolidified material in the EDG process. On the other hand, the protruded diamond grains increased the discharge interval

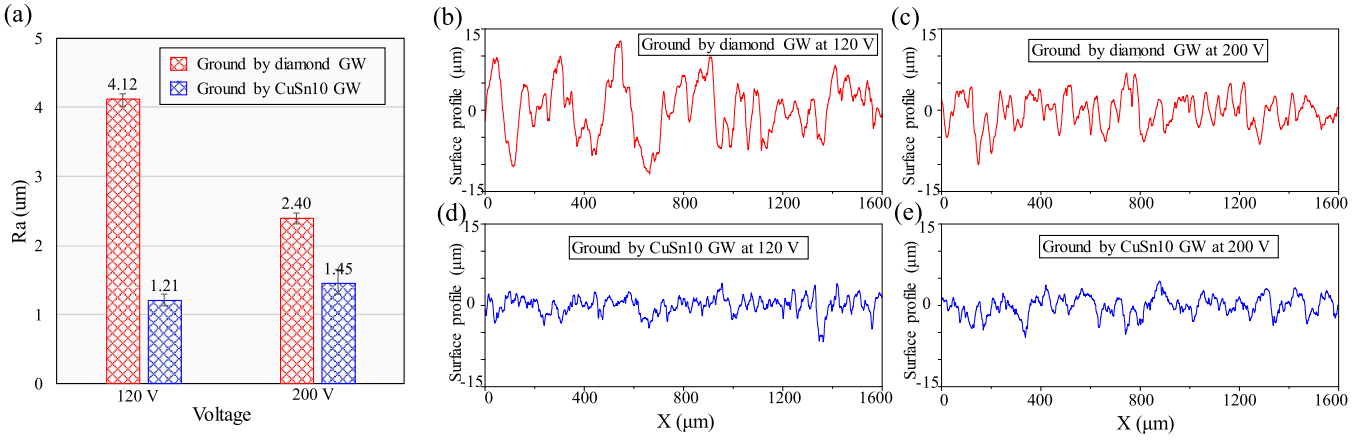

Fig. 13. Surface roughness (a) and surface profiles of the RB-SiC ground by the diamond GW (b, c) and CuSn10 alloy GW (d, e).

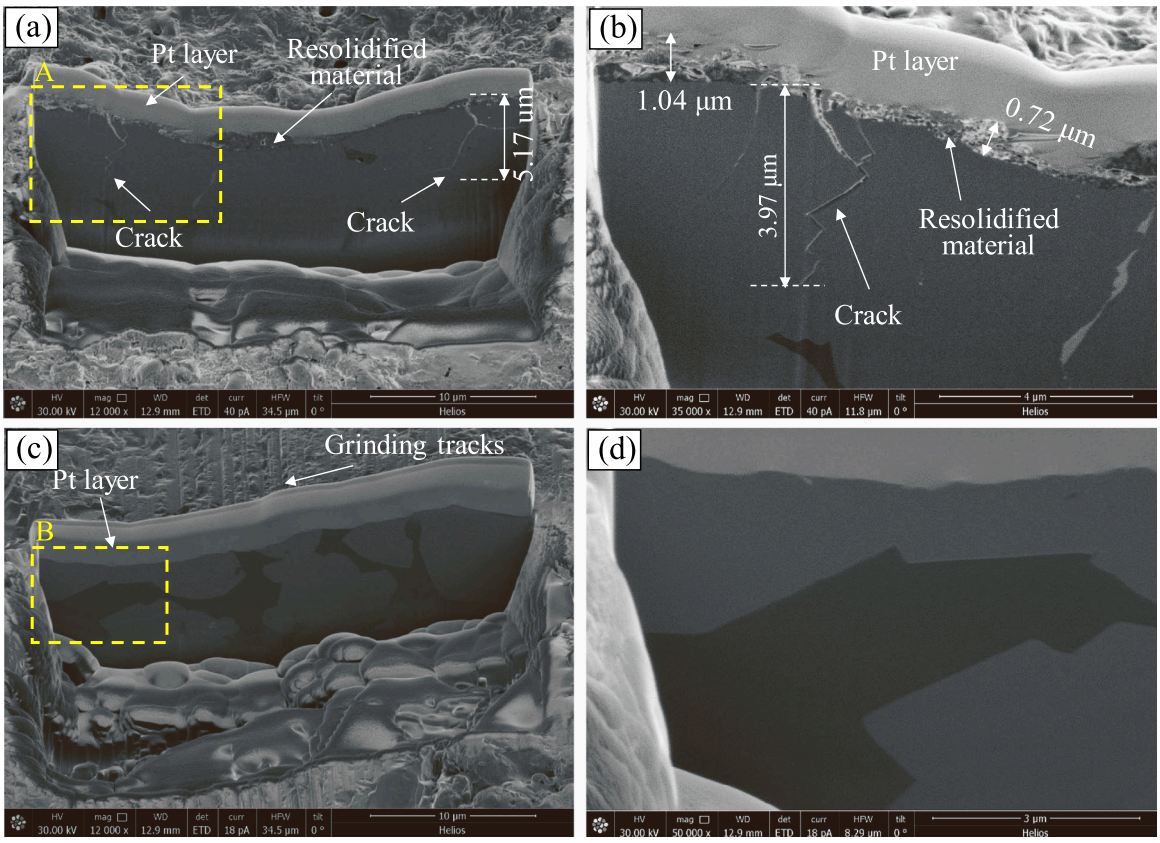

Fig. 14. Subsurface of RB-SiC ground by CuSn10 alloy GW (a, b), and by the diamond GW (c, d).

between the GW and the workpiece, resulting in a lower discharge energy and avoiding the incurrence of cracks.

4.4. *Surface topography of the as-built GWs*

The surface profiles of the as-built GWs after the EDG experiments were also measured, as shown in Fig. 15 (a1-a3). The surface profile of the CuSn10 alloy GW was still flat after the experiment, as shown in Fig. 15 (a1). The surface roughness was only 0.96 μm, indicating a steady electrical discharging machining process. Due to the existence of pores, there were several pits with various dimensions in the profile of the dressed diamond GW, as depicted in Fig. 15 (a3). Except for the pores, the Ra of the dressed diamond GW surface was around 0.49 μm. After the EDG experiment at 120 V, the Ra was increased to 4.67 μm due to tool wear caused by electrical discharge, the exposed pores, and the protruded diamond grains. As shown in Fig. 15 (b), the as-built diamond GW shows a stripe-type morphology due to the uneven tool wear caused by the ridges on the workpiece. It is inferred that the discharge process was triggered as the diamond GW contacted with the ridges of the ground RB-SiC surface, reflecting the workpiece profile on the GW surface. Diamond grains were protruded after the EDG process, which was similar to the electrical dressing process. Through the profile

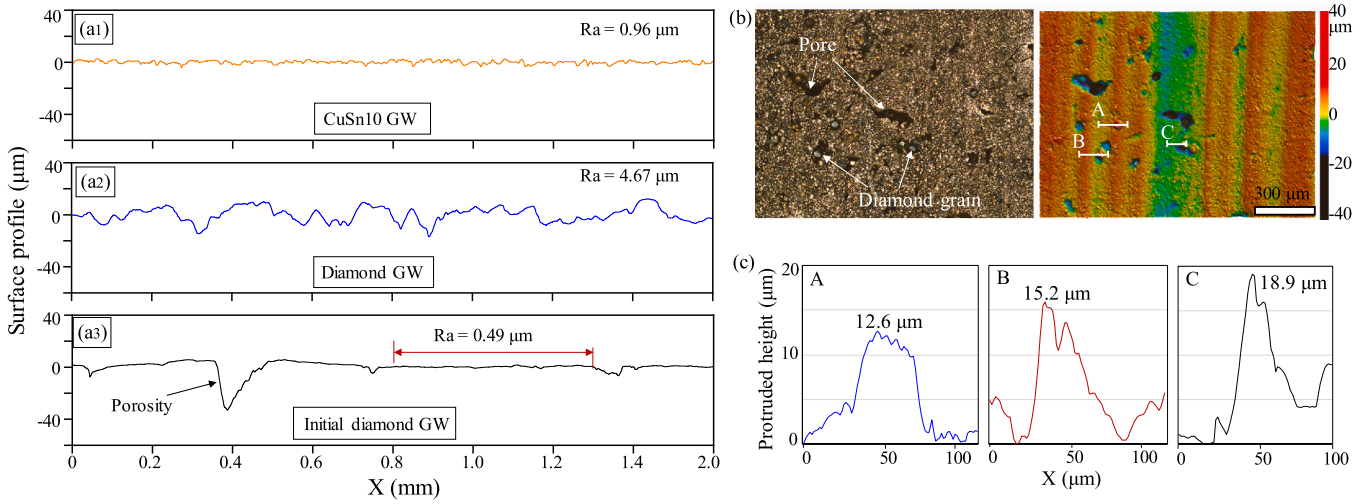

Fig. 15. (a) Surface profiles of GWs: (a1) CuSn10 alloy GW, (a2) as-built diamond GW after EDG experiments, and (a3) dressing process. (b) Surface morphology of the as-built diamond GW after the EDG experiment at 200 V. (c) Profiles of the protruded diamond grains.

measurement, the diamond grain protrusion height was in a range of 10–20 μm. Fig. 15 (c) illustrates the profiles of three protruded diamond grains in Fig. 15 (b). The protruded diamond grains could help remove the resolidified material layer on the surface.

The surface morphologies of the as-built GWs after EDG are shown in Fig. 16. A number of the resolidified sites of the bond material and discharge craters were generated on the surface, indicating that the bond material was melted by the discharge sparks. The melting of the CuSn10 alloy inevitably caused wear of the GWs. With an enhanced discharge energy, a higher temperature could cause graphitization of the diamond grains. However, no graphite was observed on the diamond grains, but a small amount of the resolidified bond material. Based on the EDS analysis, oxidation of the CuSn10 alloy hardly occurred because the GWs were fully submerged in the dielectric fluid. The G-ratio, which is defined as the ratio of workpiece removal volume V_w to GW wear volume V_s, was measured in EDG at 200 V. As shown in Fig. 16 (c), the G-ratio of diamond GW and CuSn10 alloy GW were 11.36 and 13.38, respectively. Due to the higher porosity, wear resistance of the diamond GW was slightly reduced as compared to the CuSn10 alloy GW.

5. Discussion

5.1. Formation of diamond spatters

In this study, the balling phenomenon is inferred as the main cause of the specific formation characteristics of the bronze-bond diamond GWs fabricated in LPBF. As compared to the formation of the CuSn10 alloy, the diamond grains in the mixed powders cause a significant effect on the surface morphology, porosity ratio, and flexural strength in the form of spatters. Particle spattering is generally considered to be detrimental to the quality of the built materials, because it can increase the surface roughness, enhance the porosity ratio, and introduce internal defects (Wang et al., 2020). The primary cause of spattering has been studied before and is considered as a result of the intense flow field around a melt pool (Yadroitsev et al., 2010).

Combining the formation process of the melt pool, the diamond spatters can be classified into plume-driven spatters and entrainment-driven spatters. As illustrated in Fig. 17(a), the liquid alloy in the melt pool evaporates when reaching the boiling temperature, generating a strong metal vapor jet called plume. The velocity of the plume can reach 300 m/s according to the study of (Bidare et al., 2018). The plume produces a high recoil pressure above the melt pool which causes an intense liquid alloy flow. Liquid alloy droplets may be ejected away from the melt pool by the recoil pressure, forming a so-called recoil pressure-driven spatter that is common in the fabrication of metal products (Ly et al., 2017). However, different from the fabrication of metal alloy products, diamond grains cannot be melted in the LPBF process. Thus, the diamond grains in the melt pool can be directly ejected away by the plume, resulting in the plume-driven diamond spatters. Besides, the high-speed plume drives and accelerates ambient gas toward the plume, causing an inward gas flow that entrains the surrounding particles toward the melt pool (Achee et al., 2021). Diamond grains are easier to be entrained because of the lower density. Most entrained particles are blown away by the plume and generate entrainment-driven spatters which take up a large proportion of the total spatters (Matthews et al., 2016). Therefore, plume-driven and entrainment-driven diamond spatters are the two dominant spatter forms in the fabrication of diamond GWs by LPBF.

To gain further understanding of the formation mechanisms of the plume-driven diamond spatters, an analytical model is proposed to calculate the order of force magnitude on a diamond grain in the melt pool. As depicted in Fig. 16(b), a diamond grain which is considered as a spherical particle is mainly subjected to the impact force of plume F_{im}, the retention force F_s of the melt pool, and the gravity F_g when being detached from the melt pool. The angle between F_{im} and $+Z$ direction is θ_1, and the angle between F_s and -Z direction is θ_2. The liquid flow in the melt pool is not considered in this model. The analytical model is similar to a drop of fluid in motion with another immiscible fluid, in which the diamond grain is infinitely viscous. The impact force is given by the Stokes formula (Guyon et al., 2002),

$$F_{im} = 3\pi\eta a\left(v_p - v_d\right) \tag{2}$$

where η is the gas viscosity, a is the diameter of the diamond grains (50 μm on average), v_p and v_d are the velocities of the plume and diamond grains, respectively. The gas viscosity η is around 6.9×10^{-4} g/cm/s at 3000 K (Ly et al., 2017). The plume velocity has been found to increase linearly with laser power in the study of (Bidare et al., 2018), in which the minimum velocity is 300 m/s at 50 W. The plume velocity v_p was set as 300 m/s in this study, while the initial velocity of the diamond grain v_d is zero. Therefore, the initial impact force of the plume on the diamond grain is around 9.8 μN.

The gravitational force F_g is given by an expression,

$$F_g = \frac{1}{6}\pi a^3 \rho g \tag{3}$$

The density ρ of diamond is 3.5 g/cm^3 such that the gravity is only 2.24 nN which can be neglected as compared to F_{im}. Due to the density difference with the CuSn10 alloy, a diamond grain is prone to floating on the melt pool. The retention force of the liquid CuSn10 alloy to the diamond grain F_s can be expressed as (Yazdanpanah et al., 2008),

$$F_s = \pi\sqrt{h(a-h)}\gamma\cos\varphi \tag{4}$$

where h is the wetting height and $\pi\sqrt{h(a\text{-}h)}$ is the circumference of the wetted diamond grains, as shown in Fig. 17(b). γ is the surface tension of the liquid CuSn10 alloy, and φ is the wetting angle at the contact line between the gas-liquid interface and liquid-diamond interface. Based on the wetting theory, the wetting angle is associated with surface tensions of the solid-vapor, liquid-vapor, and solid-liquid interfaces: σ_{SV} - σ_{SL} = σ_{LV} cosφ (Zhou et al., 2015). In particular, the direction of the retention force F_s is depended on the wetting angle. When φ is less than

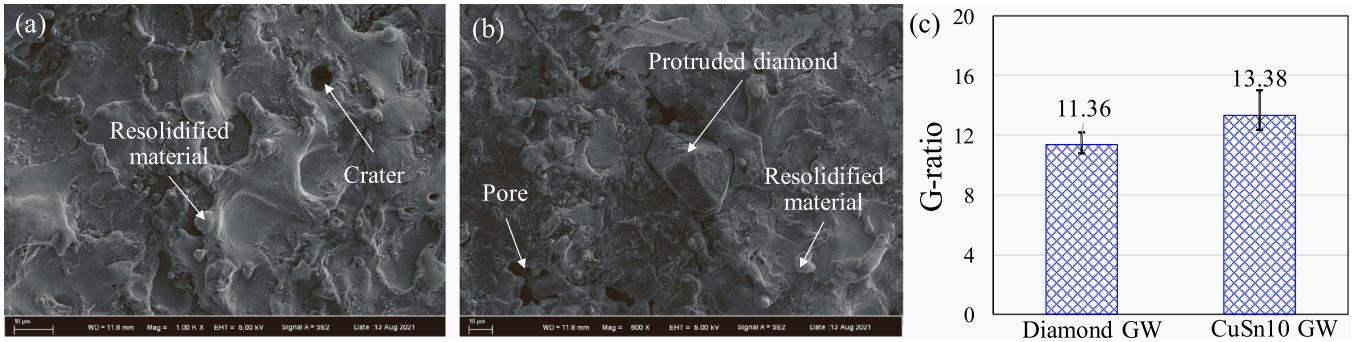

Fig. 16. Surface morphology characteristics of as-built CuSn10 alloy GW (a) and diamond GW (b), and G-ratios (c) after the EDG experiment at 200 V.

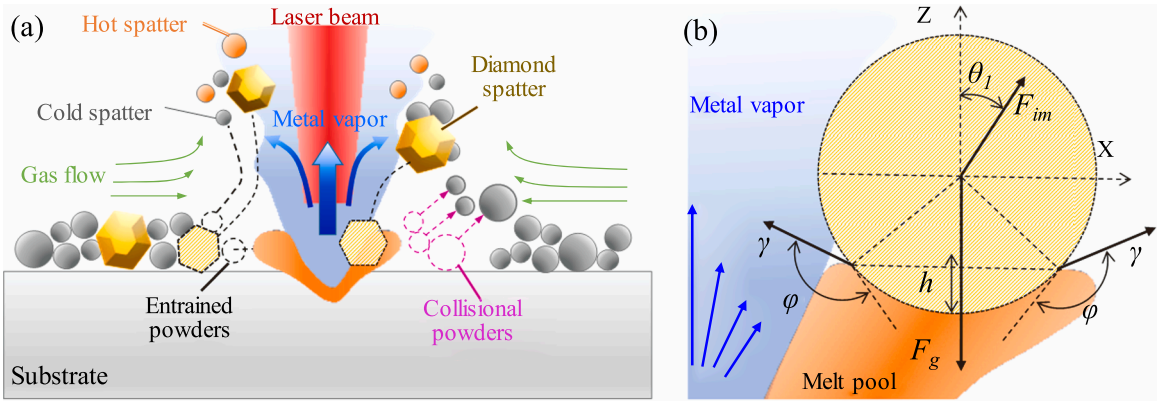

Fig. 17. (a) Schematic of the plume-driven and entrainment-driven diamond spatters; (b) sketch of the force system acting on a target diamond grain in the melt pool.

90°, the liquid can wet the solid material and the diamond grain can be pulled by the surface tension. However, the wettability of copper with diamond is poor with a wetting angle of 131.5° at 1200 °C (Dong et al., 2012), resulting in a convex shape at the contact line in Fig. 17(b). Thus, the retention force of the liquid CuSn10 alloy is negative, indicating that F_s is in the opposite direction of the gravity field which can hardly retain a diamond grain in the melt pool. Once in contact with the plume, a diamond grain in the melt pool may be ejected away unavoidably, which results in the plume-driven diamond spatter.

The formation of entrainment-driven diamond spatters is similar to that of the metal alloy powder spatters. The mixed powders in the immediate vicinity of the melt pool are entrained by a gas flow first. The entrainment force that drives the powders was modeled as the sum of turbulent lift F_{LT} and the Saffman lift due to the velocity gradient F_{LS} by (Ali and Dey, 2016), which are expressed as,

$$\left\{\begin{array}{l} F_{LT} = \dfrac{\pi^3}{4} a^3 \left(\dfrac{\partial \overline{p}_{rz}}{\partial z}\right) \\ F_{LS} = C_{LS}\rho_{ar} a^2 v_{ra} \left|\sqrt{\left(\nu \dfrac{\partial \overline{v}_{rz}}{\partial z}\right)}\right| a \end{array}\right\} \tag{5}$$

where v_r is the radial velocity field, p_{rz} is the pressure field, ν is the kinematic viscosity of argon, ρ_{ar} is the density of argon, C_{LS} is the Saffman lift coefficient. The radial velocity and velocity gradient decrease with the distance from the melt pool (Bidare et al., 2018). For the mechanics of powder laying in LPBF, a loose layer of powders is spread on the previously deposited materials. Near the melt pool, a larger velocity, velocity gradient, and pressure gradient result in a comparably larger turbulent lift and Saffman lift which draw diamond grains and alloy powders upward and toward the plume. When the entrained particles reach the plume region, they will be blown away by the impact force F_{im} as expressed in Eq. (1), resulting in the entrainment-driven spatters. Hot

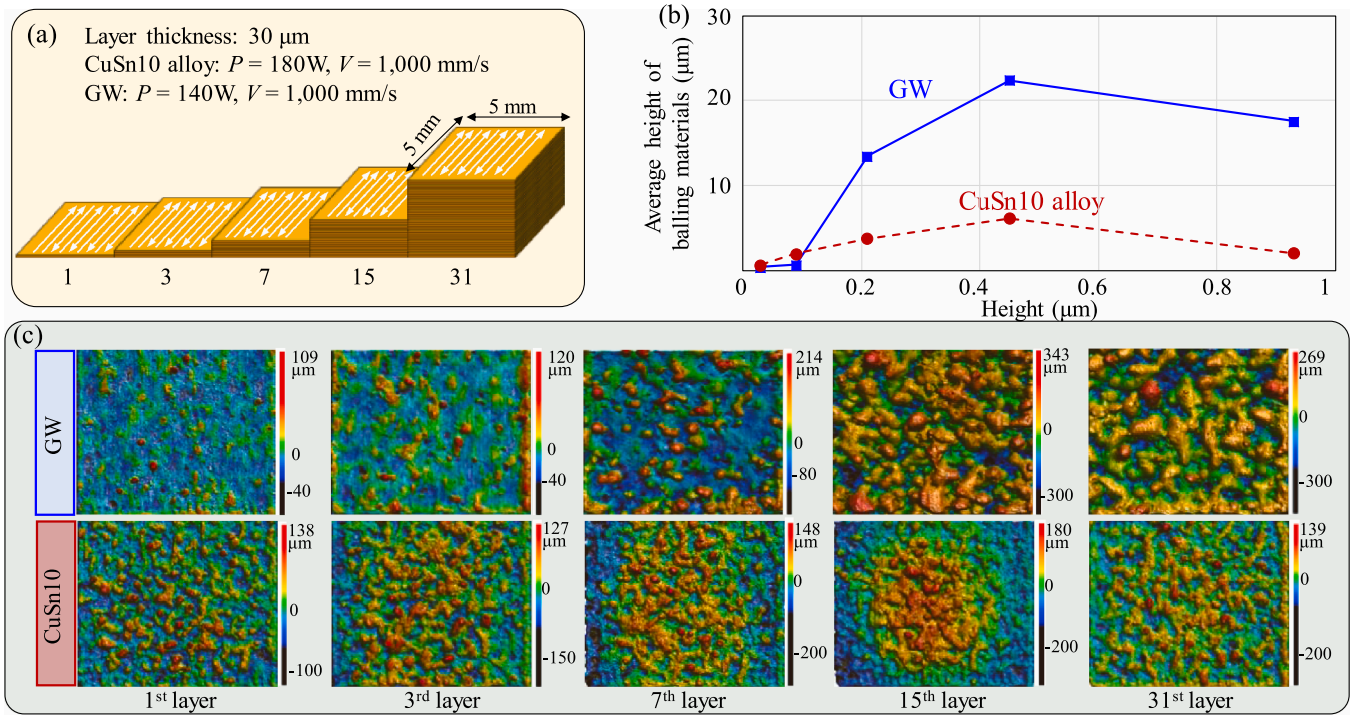

Fig. 18. Evolution of surface morphology with deposited layers: (a) schematic diagram of the diamond GW and the CuSn10 alloy specimens; (b) variation of the average height of balling materials; (c) three-dimensional surface morphology of diamond GW and CuSn10 alloy specimens at different layers.

spatters will be formed as the ejected alloy powders are melted under the irradiation of the laser beam, otherwise cold spatters will be induced (Matthews et al., 2016), as depicted in Fig. 17(a).

5.2. Effects of diamond spattering on the formation of GWs

To investigate the influence of diamond spattering on the formation characteristics, a diamond GW specimen with different heights (from one layer to 31 layers) was built, as shown in Fig. 18(a). For comparison, a similar specimen was also fabricated with the CuSn10 alloy. The morphology of each top surface was measured to investigate the evolution of balling materials, and the average height of balling materials is used to evaluate the balling level in Fig. 18(b). In the first three layers, the average height of balling materials of GW and the CuSn10 alloy specimens is at the same level. As shown in Fig. 18(c), the quantity of balling materials on the GW specimen is less than the CuSn10 specimen in the 1st and 3rd layers, because diamond spattering cause serious material loss and only a thin layer of the CuSn10 alloy was deposited. However, a surge in both the size and quantity of the balling materials occurred in the 7th layer of the GW specimen, resulting in a larger average height of balling materials in Fig. 18(b). The balling size ranges from 145 μm to 250 μm and is almost twice larger than that of the CuSn10 alloy specimen. The balling materials grow with material deposition and connect with the surrounding materials, leading to a bridging phenomenon in the 15th layer. The bridging phenomenon reduced the balling size of the 31st layer slightly, as shown in Fig. 18(b) and (c).

The evolution of balling materials on GW surface is closely related to diamond spattering, which directly influences the formation quality. On the one hand, diamond spattering induce serious material losses and produce discontinuous melt tracks. On the other hand, the homogeneity of the powder layer is greatly deteriorated by diamond spattering. The entrainment phenomenon causes a denudation zone in the surrounding powder bed around the melt track (Achee et al., 2021). In addition, as the diamond grains are ejected out of the melt pool, the surrounding powders will be collided resulting in a collision zone with few powders. Under the effect of thermal radiation, some entrained or collided alloy powders are melted partially and adhered with each other or to diamond grain, generating agglomerated powders and diamond clumps obstructing the laser path. The denudation zone, collision zone, agglomerated powders, and diamond clumps produce an uneven powder layer, leading to balling materials driven by surface tension. The following powder layer also becomes uneven because of the balling materials. Denudation and collision phenomena will become more severe in the region with a thicker powder layer, generating more balling materials and pits on the following deposited layer. Furthermore, alloy powders can be fused on the balling materials where the powder layer is relatively thinner, which makes the balling materials larger and higher. This is responsible for the surge in both size and quantity of balling materials in the 7th layer of the GW specimen. With the material deposition layer-by-layer, the balling materials continue to grow under the effect of diamond spattering until the bridging phenomenon occurs. The bridged materials form an island-like surface and reduce the height of balling materials, as depicted in Fig. 18(c).

Consequently, the balling phenomenon induced by diamond spattering plays a critical role in the formation of a diamond GW. Pores forms when the balling materials bridge with the surrounding materials and the porosity ratio is increased with the balling size. With a higher laser energy density, diamond spattering will become more serious and increase the balling size due to a more intense plume and gas flow, resulting in an increased porosity ratio but a decreased flexural strength of the diamond GW.

5.3. Performance of as-built diamond GW in EDG

As observed in the surface profiles and subsurface quality, the RB-SiC was removed by the combined effect of the electrical discharge and grinding processes. Although the surface quality of the RB-SiC ground by the CuSn10 alloy GW was better, resolidified material and cracks were generated in the subsurface. The diamond grinding could mechanically remove the resolidified layer through cutting, plowing, or sliding with the as-built diamond GW, thus reducing the subsurface damage of RB-SiC. Bond materials were also evaporated and melted under the thermal effect of discharge sparks, resulting in the protruded diamond grains. Due to the higher porosity, the G-ratio of the as-built diamond GW was slightly lower than the CuSn10 alloy wheel. Overall, the diamond GW fabricated by LPBF could enhance the subsurface quality of SiC.

6. Conclusions

In this study, the effect of spattering on the formation mechanisms of MMCs in LPBF is investigated by taking diamond GWs as an example. The processing parameters (laser power and scanning velocity) exert a significant influence on the formation quality and mechanical properties of the as-built GWs due to the balling phenomenon. In the LPBF of MMCs with such coarse reinforcements, spattering plays a vital role in the incurrence of the balling phenomenon. Furthermore, the grinding performance of the as-built diamond GW on RB-SiC is evaluated and compared with a CuSn10 GW in terms of surface quality. The following conclusions can be drawn:

(1) The formation characteristics of MMCs in LPBF are closely associated with the balling phenomenon. Different from that of the CuSn10 alloy, the porosity ratio of the as-built GWs is increased slightly with the increasing LED due to the increased balling materials. The flexural strength of GWs decreases with the porosity ratio, and the maximum flexural strength reaches 213 MPa.
(2) Both the plume-driven and entrainment-driven diamond spatters are easily triggered in LPBF due to the weak retention force applied by the melt pool and entrainment force caused by the ambient gas flow. Spattering directly affects the quality of the melt track and powder layer and is the dominant cause of balling phenomenon for MMCs with such coarse reinforcement particles. The size and quantity of balling materials first increase and then decrease slightly with deposition height.
(3) Even though the surface ground by the as-built diamond GW is rougher than that by the CuSn10 alloy GW, the introduced grinding process of the diamond grains can remove the resolidified layer and suppress the generation of cracks in the EDG of RB-SiC.

CRediT authorship contribution statement

Shuai Li: Conceptualization, Methodology, Investigation, Writing – original draft, Writing – review & editing. **Qinghong Jiang:** Investigation, Software. **Sai Guo:** Investigation, Methodology. **Bi Zhang:** Conceptualization, Supervision, Funding acquisition, Writing – review & editing. **Cong Zhou:** Conceptualization, Writing – review & editing.

Declaration of Competing Interest

The authors declare that they have no known competing financial interests or personal relationships that could have appeared to influence the work reported in this paper.

Acknowledgments

This work was supported by Shenzhen Key Laboratory of Cross-Scale Manufacturing Mechanics of Southern University of Science and Technology, China under ZDSYS20200810171201007, and by Shenzhen

Science and Technology Innovation Commission of China for the projects numbered JSGG20210420091802007 and KQTD20190929172505711. This work was also supported by the Pico Center at SUSTech with support from the Presidential Fund and Development and Reform Commission of Shenzhen Municipality, China. Li Shuai acknowledges Dr. Zhao Yonghua and Guan Junming at Department of Mechanical and Energy Engineering, SUSTech, for providing the EDG equipment and instructions. The authors also wish to acknowledge the assistance from SUSTech Core Research Facilities, China.

References

Achee, T., Guss, G., Elwany, A., Matthews, M., 2021. Laser pre-sintering for denudation reduction in the laser powder bed fusion additive manufacturing of Ti-6Al-4V alloy. Addit. Manuf. 42. https://doi.org/10.1016/j.addma.2021.101985.

Ali, S.Z., Dey, S., 2016. Hydrodynamics of sediment threshold. Phys. Fluids 28. https://doi.org/10.1063/1.4955103.

Bidare, P., Bitharas, I., Ward, R.M., Attallah, M.M., Moore, A.J., 2018. Fluid and particle dynamics in laser powder bed fusion. Acta Mater. 142. https://doi.org/10.1016/j.actamat.2017.09.051.

Constantin, L., Kraiem, N., Wu, Z., Cui, B., Battaglia, J.L., Garnier, C., Silvain, J.F., Lu, Y. F., 2021. Manufacturing of complex diamond-based composite structures via laser powder-bed fusion. Addit. Manuf. 40. https://doi.org/10.1016/j.addma.2021.101927.

Denkena, B., Krödel, A., Harmes, J., Kempf, F., Griemsmann, T., Hoff, C., Hermsdorf, J., Kaierle, S., 2020. Additive manufacturing of metal-bonded grinding tools. Int. J. Adv. Manuf. Technol. 107. https://doi.org/10.1007/s00170-020-05199-9.

Ding, W.F., Xu, J.H., Chen, Z.Z., Yang, C.Y., Song, C.J., Fu, Y.C., 2013. Fabrication and performance of porous metal-bonded CBN grinding wheels using alumina bubble particles as pore-forming agents. Int. J. Adv. Manuf. Technol. 67. https://doi.org/10.1007/s00170-012-4567-4.

Dong, Y., Zhang, R., He, X., Ye, Z., Qu, X., 2012. Fabrication and infiltration kinetics analysis of Ti-coated diamond/copper composites with near-net-shape by pressureless infiltration. Mater. Sci. Eng.: B. https://doi.org/10.1016/j.mseb.2012.08.009.

Du, Z. jun, Zhang, F. lin, Xu, Q. sheng, Huang, Y. jie, Li, M. cong, Huang, H. ping, Wang, C. yong, Zhou, Y. mei, Tang, H. qun, 2019. Selective laser sintering and grinding performance of resin bond diamond grinding wheels with arrayed internal cooling holes. Ceram. Int. 45. https://doi.org/10.1016/j.ceramint.2019.07.076.

Gan, J., Gao, H., Wen, S., Zhou, Y., Tan, S., Duan, L., 2020. Simulation, forming process and mechanical property of Cu-Sn-Ti/diamond composites fabricated by selective laser melting. Int. J. Refract. Met. Hard Mater. 87. https://doi.org/10.1016/j.ijrmhm.2019.105144.

Guyon, E., Hulin, J.-P., Petit, L., Mitescu, C., Jankowski, D., 2002. Physical hydrodynamics. Appl. Mech. Rev. 55. https://doi.org/10.1115/1.1497485.

Hojjatzadeh, S.M.H., Parab, N.D., Yan, W., Guo, Q., Xiong, L., Zhao, C., Qu, M., Escano, L.I., Xiao, X., Fezzaa, K., Everhart, W., Sun, T., Chen, L., 2019. Pore elimination mechanisms during 3D printing of metals. Nat. Commun. 10. https://doi.org/10.1038/s41467-019-10973-9.

Khairallah, S.A., Anderson, A.T., Rubenchik, A., King, W.E., 2016. Laser powder-bed fusion additive manufacturing: physics of complex melt flow and formation mechanisms of pores, spatter, and denudation zones. Acta Mater. 108. https://doi.org/10.1016/j.actamat.2016.02.014.

Khmyrov, R.S., Safronov, V.A., Gusarov, A.V., 2016. Obtaining crack-free WC-Co alloys by selective laser melting. Phys. Procedia. https://doi.org/10.1016/j.phpro.2016.08.091.

Kumar, S., Czekanski, A., 2017. Optimization of parameters for SLS of WC-Co. Rapid Prototyp. J. 23. https://doi.org/10.1108/RPJ-10-2016-0168.

Li, H.N., Axinte, D., 2016. Textured grinding wheels: a review. Int. J. Mach. Tools Manuf. 109. https://doi.org/10.1016/j.ijmachtools.2016.07.001.

Li, S., Zhang, B., Jiang, Q., Han, H., Wen, J., Zhou, C., 2022. Formation characteristics of nickel-based diamond abrasive segment by selective laser melting. Opt. Laser Technol. 148, 107665 https://doi.org/10.1016/j.optlastec.2021.107665.

Li, S., Zhou, Z., Mo, B., Deng, Z., 2021. Study on forming processes for laser brazing of multilayer diamond grains and Ni-Cr alloy. Zhongguo Jixie Gongcheng/China Mech. Eng. 32. https://doi.org/10.3969/j.issn.1004-132X.2021.08.011.

Li, S.C., Zhou, Z.H., Mo, B., Deng, Z.H., 2021. Microscopic bonding morphology of laser brazing multilayer diamond grains with Ni-Cr alloy. Cailiao Rechuli Xuebao/transactions mater. Heat. Treat. 42. https://doi.org/10.13289/j.issn.1009-6264.2021-0033.

Li, Y., Dai, Q., Tang, Y., 2011. Research on the new porous metal bond for diamond wheel. Jingangshi yu Moliao Moju Gongcheng/Diam. Abras. Eng. 31. https://doi.org/10.3969/j.issn.1006-852X.2011.05.018.

Ly, S., Rubenchik, A.M., Khairallah, S.A., Guss, G., Matthews, M.J., 2017. Metal vapor micro-jet controls material redistribution in laser powder bed fusion additive manufacturing. Sci. Rep. 7. https://doi.org/10.1038/s41598-017-04237-z.

Ma, Y., Ji, G., Li, X.P., Chen, C.Y., Tan, Z.Q., Addad, A., Li, Z.Q., Sercombe, T.B., Kruth, J. P., 2019. On the study of tailorable interface structure in a diamond/Al12Si composite processed by selective laser melting. Materialia 5. https://doi.org/10.1016/j.mtla.2019.100242.

Mao, Z., Zhang, D.Z., Jiang, J., Fu, G., Zhang, P., 2018. Processing optimisation, mechanical properties and microstructural evolution during selective laser melting of Cu-15Sn high-tin bronze. Mater. Sci. Eng. A 721. https://doi.org/10.1016/j.msea.2018.02.051.

Matthews, M.J., Guss, G., Khairallah, S.A., Rubenchik, A.M., Depond, P.J., King, W.E., 2016. Denudation of metal powder layers in laser powder bed fusion processes. Acta Mater. 114. https://doi.org/10.1016/j.actamat.2016.05.017.

Rao, X., Zhang, F., Li, C., Li, Y., 2018. Experimental investigation on electrical discharge diamond grinding of RB-SiC ceramics. Int. J. Adv. Manuf. Technol. 94. https://doi.org/10.1007/s00170-017-1102-7.

Rao, X., Zhang, F., Lu, Y., Luo, X., Chen, F., 2020. Surface and subsurface damage of reaction-bonded silicon carbide induced by electrical discharge diamond grinding. Int. J. Mach. Tools Manuf. 154. https://doi.org/10.1016/j.ijmachtools.2020.103564.

Sharma, D.K., Mahant, D., Upadhyay, G., 2019. Manufacturing of metal matrix composites: a state of review. Mater. Today: Proc. https://doi.org/10.1016/j.matpr.2019.12.128.

Spierings, A.B., Leinenbach, C., Kenel, C., Wegener, K., 2015. Processing of metal-diamond-composites using selective laser melting. Rapid Prototyp. J. 21. https://doi.org/10.1108/RPJ-11-2014-0156.

Tian, C., Li, X., Chen, Z., Guo, G., Wang, L., Rong, Y., 2020. Study on formability, mechanical property and finite element modeling of 3D-printed composite for metal-bonded diamond grinding wheel application. J. Manuf. Process 54. https://doi.org/10.1016/j.jmapro.2020.02.028.

Tian, C., Li, X., Li, H., Guo, G., Wang, L., Rong, Y., 2019. The effect of porosity on the mechanical property of metal-bonded diamond grinding wheel fabricated by selective laser melting (SLM). Mater. Sci. Eng. A 743. https://doi.org/10.1016/j.msea.2018.11.138.

Tian, C., Li, X., Zhang, S., Guo, G., Wang, L., Rong, Y., 2018. Study on design and performance of metal-bonded diamond grinding wheels fabricated by selective laser melting (SLM). Mater. Des. 156. https://doi.org/10.1016/j.matdes.2018.06.029.

Traxel, K.D., Bandyopadhyay, A., 2021. Diamond-reinforced cutting tools using laser-based additive manufacturing. Addit. Manuf. 37. https://doi.org/10.1016/j.addma.2020.101602.

Traxel, K.D., Bandyopadhyay, A., 2019. First demonstration of additive manufacturing of cutting tools using directed energy deposition system: stelliteTM-based cutting tools. Addit. Manuf. 25. https://doi.org/10.1016/j.addma.2018.11.019.

Wang, D., Ye, G., Dou, W., Zhang, M., Yang, Y., Mai, S., Liu, Y., 2020. Influence of spatter particles contamination on densification behavior and tensile properties of CoCrW manufactured by selective laser melting. Opt. Laser Technol. 121. https://doi.org/10.1016/j.optlastec.2019.105678.

Wang, J., Zhou, X.L., Li, J., Brochu, M., Zhao, Y.F., 2020. Microstructures and properties of SLM-manufactured Cu-15Ni-8Sn alloy. Addit. Manuf. 31. https://doi.org/10.1016/j.addma.2019.100921.

Wang, L., Li, J., Catalano, M., Bai, G., Li, N., Dai, J., Wang, X., Zhang, H., Wang, J., Kim, M.J., 2018. Enhanced thermal conductivity in Cu/diamond composites by tailoring the thickness of interfacial TiC layer. Compos. Part A Appl. Sci. Manuf. 113. https://doi.org/10.1016/j.compositesa.2018.07.023.

Wu, J., Zhang, S., Qu, F., Zhou, H., Tang, J., 2019. Matrix material for a new 3D-printed diamond-impregnated bit with grid-shaped matrix. Int. J. Refract. Met. Hard Mater. 82. https://doi.org/10.1016/j.ijrmhm.2019.04.017.

Yadroitsev, I., Gusarov, A., Yadroitsava, I., Smurov, I., 2010. Single track formation in selective laser melting of metal powders. J. Mater. Process. Technol. 210. https://doi.org/10.1016/j.jmatprotec.2010.05.010.

Yang, Z., Zhang, M., Zhang, Z., Liu, A., Yang, R.Y., Liu, S., 2016. A study on diamond grinding wheels with regular grain distribution using additive manufacturing (AM) technology. Mater. Des. 104. https://doi.org/10.1016/j.matdes.2016.04.104.

Yazdanpanah, M.M., Hosseini, M., Pabba, S., Berry, S.M., Dobrokhotov, V.V., Safir, A., Keynton, R.S., Cohn, R.W., 2008. Micro-wilhelmy and related liquid property measurements using constant-diameter nanoneedle-tipped atomic force microscope probes. Langmuir 24. https://doi.org/10.1021/la802820u.

Zhao, B., Ding, W., Chen, Z., Yang, C., 2019. Pore structure design and grinding performance of porous metal-bonded CBN abrasive wheels fabricated by vacuum sintering. J. Manuf. Process 44. https://doi.org/10.1016/j.jmapro.2019.06.001.

Zhou, X., Liu, X., Zhang, D., Shen, Z., Liu, W., 2015. Balling phenomena in selective laser melted tungsten. J. Mater. Process. Technol. 222. https://doi.org/10.1016/j.jmatprotec.2015.02.032.

Zhou, Y., Ding, W., Zhao, B., 2020. Effect of pore structure and distribution of porous metal bonded CBN wheel on mechanical properties of abrasive layer matrix. Jingangshi yu Moliao Moju Gongcheng/Diamond Abrasives Eng. 40 https://doi.org/10.13394/j.cnki.jgszz.2020.2.0005.